Multi-fluorescence high-resolution episcopic microscopy (MF-HREM) for three dimensional imaging of adult murine organs

Claire Walsh[1], Natalie Holroyd[1], Eoin Finnerty[1], Sean G. Ryan[2], Paul W. Sweeney[3,4], Rebecca J. Shipley[4], Simon Walker-Samuel[1].

1. Centre for Advanced Biomedical Imaging, University College London, 72 Huntley Street, London, WC1E 6DD, UK. **2.** School of Physics, Astronomy and Mathematics, University of Hertfordshire, College Lane, Hatfield, AL10 9AB, UK. **3.** Cancer Research UK Cambridge Institute, University of Cambridge, Li Ka Shing Centre, Cambridge, CB2 0RE, UK **4.** Department of Mechanical Engineering, University College London, London, UK

Abstract

Three-dimensional microscopy of large biological samples (>0.5 cm^3) is transforming biological research. Many existing techniques require trade-offs between image resolution and sample size, require clearing or use optical sectioning. These factors complicate the implementation of large volume 3D imaging. Here we present Multi-fluorescent High Resolution Episcopic Microscopy (MF-HREM) which allows 3D imaging of large samples without the need for clearing or optical sectioning.

MF-HREM uses serial-sectioning and block-facing wide-field fluorescence, without the need for tissue clearing or optical sectioning. We detail developments in sample processing including stain penetration, resin embedding and imaging. In addition, we describe image post-processing methods needed to segment and further quantify these data. Finally, we demonstrate the wide applicability of MF-HREM by: 1) quantifying adult mouse glomeruli. 2) identifying injected cells and vascular networks in tumour xenograft models; 3) quantifying vascular networks and white matter track orientation in mouse brain.

Introduction

Immunohistochemistry has traditionally been the primary method used to image specific proteins and structures in large (>1cm^3) tissue samples. However, the two-dimensional nature of conventional histological slices means that the complete, and often complex, three-dimensional structure of biological tissues generally cannot be captured and investigated. Numerous efforts have been made to simplify the three-dimensional (3D) alignment of serial histological sections, but have proved to be non-trivial due to the significant distortions and misalignments that occur during sectioning and processing (1). To meet this need, several 3D fluorescent imaging techniques have been developed that are now providing data over length scales from single cells to tissues, organs and organisms (2).

As with many fluorescent imaging techniques, multiplexed fluorescence staining is a particularly powerful tool for evaluating spatial relationships between features, often enabling function to be inferred (3–5).

All 3D microscopy techniques must overcome the opacity of biological tissue caused by optical scatter of tissue structures. Approaches to this can be grouped into two categories: clearing-based, where the tissue is rendered optically transparent through de-lipidation and refractive index matching (6–8)(9); and serial sectioning, where the entire sample is physically cut.

43 Cleared samples can be imaged using techniques such as light-sheet microscopy (2,4,7)
44 and optical projection tomography (OPT) (10,11). However, clearing requires often complex,
45 lengthy and costly tissue preparation, with variable efficacy (9,12), and widely acknowledged
46 morphological changes to the sample (9,13). Additionally, sample size is limited by the
47 working distance of the microscope objective lens (7) and the objective lens must be
48 protected from the often corrosive clearing solutions. Resolution is also limited by the need
49 for broader light sheets to penetrate greater tissue depth (14).

50 Block-facing serial-sectioning, overcomes slice alignment issues by imaging the
51 surface of the exposed sample after each successive cut thereby creating an inherently
52 aligned image stack and removing the need to retain the structural integrity of individual
53 slices (Figure 1B). However, block-face imaging can suffer from loss of optical resolution in
54 the z-axis, due to contamination by out of focus light from below the block surface (shine-
55 through) (15). The addition of optical-sectioning capabilities such as two-photon and
56 structured illumination into serial sectioning instruments has aimed to overcome this issue
57 (3), (14), (16) (13,17), but at the cost of dramatically increasing the technical requirements
58 for the imaging instrument require high powered lasers and often they are custom built.
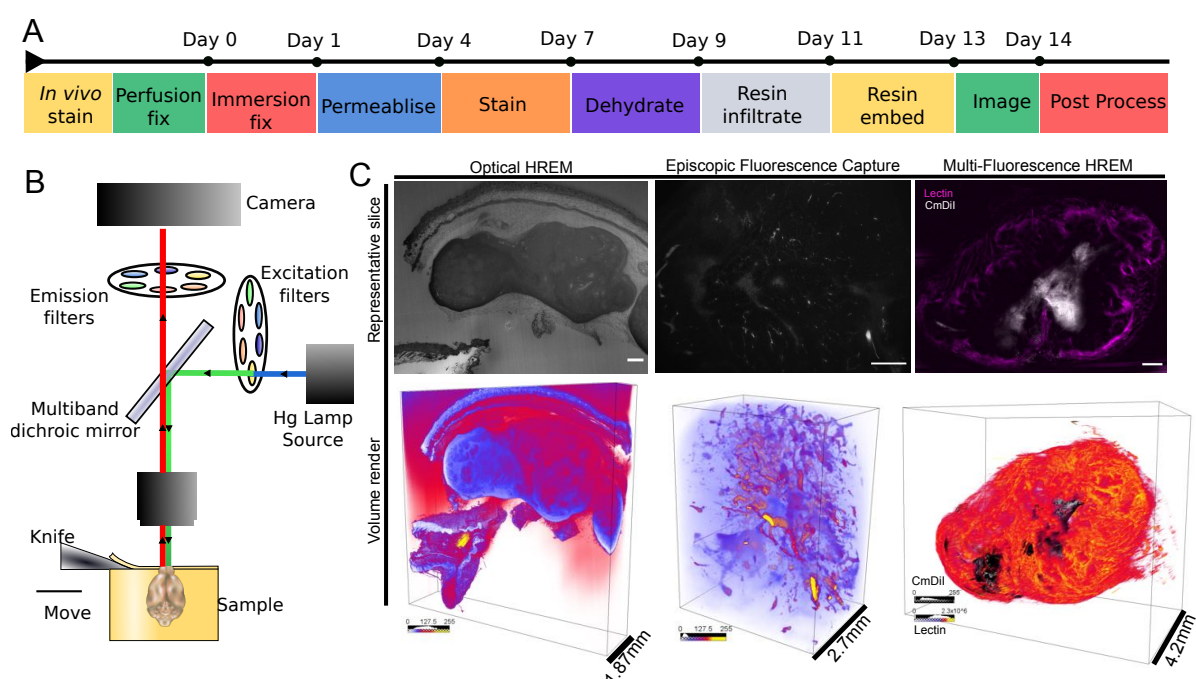
59

Figure 1. The MF-HREM acquisition pipeline. A) Shows the MF-HREM sample preparation, acquisition and image post-processing timeline for a typical multi-stained sample. For animal models, the sample is collected following perfusion fixation. In some cases the sample is collected following perfusion fixation, in some cases the sample is stained in vivo, prior to fixation. The sample is fixed overnight in PFA before being whole-mount stained (small mount stain or antibody). As almost all candidate resins are immiscible with water, samples must be dehydrated before polymerisation. Once staining is complete, the sample is dehydrated using a series of organic solvents, followed by infiltration with a three-part glycol methanlacrylate acrylic (GMA) resin. Finally, the sample is set within the final resin block in the desired orientation and attached to a chuck for mounting to the instrument. Sample imaging with multiple wavelength channels is automated. B) The Optical HREM instrument (Indigo Scientific, UK) consists of a fluorescent stereomicroscope with 1x objective lens (NA:0.25), and a variable zoom which provides fields of view ranging from 25 mm down to 2.3 mm. Biological samples are held within a removable sample holder under the microscope objective on a z-translational stage to enable sections to be cut with a horizontally-aligned, automated sectioning blade. Single-use tungsten carbide blades allow large samples to be cut. The sample is illuminated by a mercury vapour lamp, with separate excitation and emission filters for multiple wavelength imaging. C) Comparison of previously developed optical HREM, Episcopic fluorescent microscopy and MF-HREM on subcutaneously grown xenograft colorectal cancer tumours. Optical HREM uses Eosin B for contrast, Episcopic fluorescent microscopy uses tissue autofluorescence, while MF-HREM has used multiplexed staining of tumour vasculature and injected cells. In the case of Optical HREM, it is difficult to definitively identify any particular tumour features due to the widespread binding of Eosin B. In the autofluorescence case, blood has been left in the tumour to enhance vessel autofluorescence; whilst this appears to have been effective, it is difficult to conclusively identify bright structures and blood vessels, and only one fluorescence channel can be imaged. MF-HREM demonstrates clear vascular structure as stained by i.v administered lectin and initially injected cells can be clearly identified via the medium-term cell tracing dye CM-DiI. Scale bars are 500μm on 2D slices.

60

61

62 The HREM method was originally developed as a high-throughput platform for phenotyping
63 transgenic mouse models (18–20). It was subsequently used to map gene expression (via

64 lacZ) (21), and for analysis of human tissue (22,23), and developed into a commercial
65 instrument – Optical HREM (Indigo Scientific, UK). In these studies, the source of image
66 contrast was eosin blocking (i.e. the property of eosin, when bound to eosinophilic proteins,
67 to inhibit the fluorescence of unbound eosin in the embedding resin). This produces images
68 with an appearance similar to the inverse of a traditional eosin staining in histology (shown in
69 Figure 1C). Previously, studies have also embedded samples in (non-fluorescent) resin and
70 used the native autofluorescence of the tissue as a source of contrast (20). This technique
71 has only been published as applied to mouse embryos and has no potential to target specific
72 structures or multiplex stains (shown in Figure 1C). Moreover, the resolution is far coarser
73 than Eosin stained HREM as no post-processing solutions to recover the axial resolution
74 have been developed (24).
75   Here, we describe the development of *multi-fluorescent* high resolution episcopic
76 microscopy (MF-HREM), this technique allows multiplexed fluorescent imaging of large
77 tissue samples, at high resolution, without the need to perform tissue clearing, optical
78 sectioning or custom build an instrument. MF-HREM is a block-facing serial sectioning
79 imaging technique (21,25), in which samples are embedded in resin and sectioned within the
80 body of a microscope using an automated microtome blade. Wide-field multi-channel
81 fluorescent images of the block face are acquired after every section, resulting in an
82 inherently aligned stack of 3D fluorescent images (See Figure 1B).
83 MF-HREM offers a convenient solution to the difficulties associated with the alignment of
84 traditional histological sections, and has enabled, for the first time, the extension of HREM to
85 provide multiplexed fluorescence images with targeted labelling. This included the
86 development of a MF-HREM tissue-processing, acquisition and post-processing pipeline,
87 with the use of an opacifying agent and image deconvolution to recover axial image
88 resolution. As MF-HREM does not need tissues to be optically cleared, it is advantageous
89 for imaging tissue morphology (13) and can be used in conjunction with lipophilic dyes that
90 cannot be used in solvent based clearing (26,27). For MF-HREM, lateral resolution is
91 determined directly by the microscope objective, while axial resolution is related to both
92 section thickness and light penetration into the block. As the block is physically sliced there
93 is no inherent link between sample depth and resolution. A diagram of the MF-HREM
94 pipeline is shown in Figure 1A.
95   Having developed a pipeline for preparing samples, acquiring data and image post-
96 processing we then used MF-HREM to investigate the structure of three biological systems:
97 1) glomeruli in adult mouse kidneys; 2) blood vessels in a mouse tumour xenograft model;
98 and 3) cerebral vasculature and white matter tract orientation in a mouse brain.
99 We show here that these developments greatly broaden the potential applications of HREM
100 and provide a large-volume 3D imaging platform that is accessible to a wide range of
101 researchers.
102
103
104 **Results**
105
106 **Comparison of embedding resins for MF-HREM**
107 MF-HREM requires samples to be embedded within a hard resin, to provide mechanical
108 stability (stiffness) during sectioning. Various commercially-available resins are used in
109 histology, however as these resins are designed to be manually cut and subsequently
110 stained, they are not optimised for automated, thin sectioning, fluorescence preservation or,
111 in many cases, large samples (28,29). We selected five commercial resins based on the

112   literature which covered the three broad chemical categories for hard resins: methacrylate
113   resins - Technovit 7100, Technovit 8100 and Lowicryl HM20; epoxy resin – Spurr; and
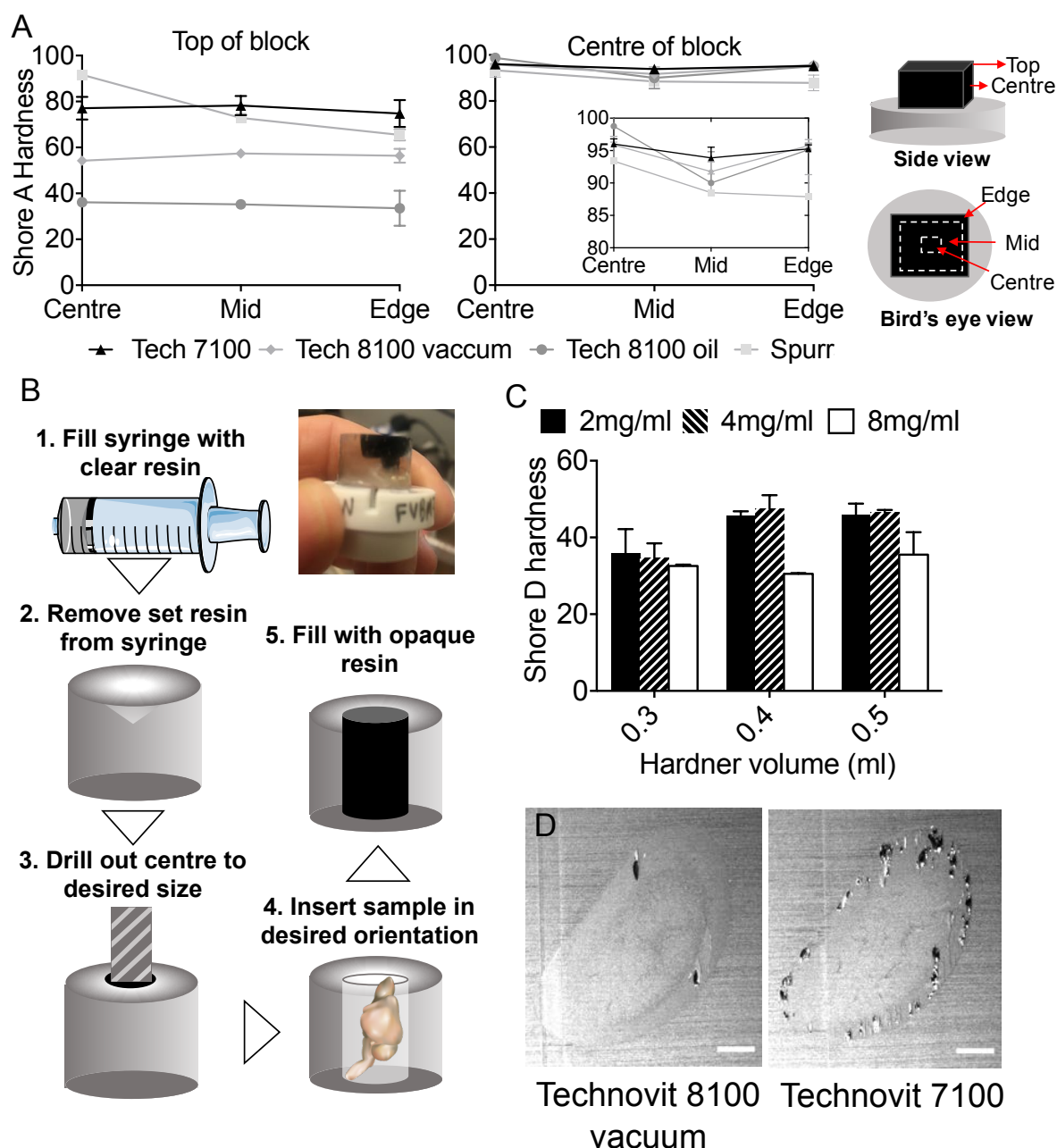114   arcylic resins – LR White (28,30–32).
115

Figure 2. Characterisation of potential resins and optimisation of embedding procedure. A) Hardness measurements for 3 candidate resins (Technovit 7100, Technovit 8100 and Spurr with Technovit 8100 under two different oxygen exclusion conditions: oil or vacuum. Hardness measurements were made using a Shore Duromenter A at two axial positions: top surface and block centre, and at 3 lateral positions for each axial: centre, mid and edge (as indicated in the diagram. Measurements were made in triplicate on two independent samples for each case (mean and standard deviation shown. Comparing the two graphs show that all samples had greater hardness at the centre of the block than the top of the block and at each axial position there was a gradient of decreasing hardness for Spurr resin from the centre to the edge. Technovit 8100 set under oil had the lowest hardness at the top of the block but in the centre all resins had similar measured hardness. B) Diagram showing the simple procedure for embedding samples in known orientation with Orasol Black whilst ensuring the correct FOV can be set at imaging. C) Hardness measurements for Technovit 8100 set under vacuum with three different amounts of secondary catalyst (0.3, 0.4 or 0.5 mL per 15 mL of infiltration soln.) and Orasol Black (2,4,8 mg/mL). Hardness was measured on the top of the block (axially) and in the centre of the block (laterally) with 2 replicate measures on two independent samples in each case. Results show a significant increase in hardness with increasing secondary catalyst and decreasing concentration of Orasol Black (Two-way anova p=0.0059 for secondary catalyst p=0.0011 for opacifying agent concentration.) D) Representative images of two samples embedded in Technovit 8100 and Technovit 7100, showing the flaky resin/voids that can be encountered more so for Technovit 7100 (scale bar =1mm).

116
117

118 For each resin chemical setting options rather than heat or UV were used (see methods for
119 more details). For resins requiring low oxygen to set (Technovit 8100) both setting under
120 vacuum and setting under a mineral oil layer were investigated (see methods for further
121 details).
122   Resins were initially assessed for the time taken to set with and without an opacifying
123 agent Orasol Black (see Supplementary table). LR White and Lowicryl HM20 were excluded
124 from further testing due to expansion during setting and slow setting (>120 hrs) respectively.
125 For the remaining resins — Technovit 8100, 7100 and Spurr — automated cutting
126 consistency and image quality were assessed. During automated cutting with the HREM,
127 Spurr blocks either chipped or broke. Comparisons of cut quality with embedded tissue for
128 Technovit 7100 and 8100 showed Technovit 7100 to have an increased incidence of 'flaky'
129 resin (i.e. where resin had not fully set in the centre of the block or voids were evident) (see
130 Figure 2B).
131 Hardness testing of Technovit 8100 (oil or vacuum), 7100 and Spurr (Figure 2A) showed
132 that the top of the block was less hard than the centre of the block for all resins. For
133 Technovit 8100 blocks were harder when set with vacuum by comparison to mineral oil. It
134 was also notable that Spurr resin demonstrated a gradient of hardness from the edge of the
135 section to the centre.
136 Based on the above results Technovit 8100 was chosen as the candidate resin and the final
137 stage of resin optimisation focused on quantifying and tuning the properties of Technovit
138 8100 based on the amount of secondary catalyst and Orasol Black (see Figure 2C).
139 Increasing the volume of secondary catalyst or decreasing the concentration of opacifying
140 agent significantly increased hardness (Two-way anova p=0.0059 for secondary catalyst
141 p=0.0011 for opacifying agent concentration.)
142 Based on these results, embedding protocols for various adult murine tissues, in Technovit
143 8100, were established and are shown in Table 1.

Reagent	Embryo (upto E12.5) Organoid or 3D culture	Small adult organ e.g. nerve, mammary gland, brain hemisphere or embryo E14.5 to P1	Large adult mouse organ Heart, Liver, Kidney, Whole brain, subcutaneous tumour, lung	Human biopsy material (greater than 1.5 cm^3) OR highly fibrous tissue
Acetone 50%	1hr	6hrs	12hrs	24 hrs (refresh at 12hrs)
Acetone 70%	1hr	6hrs	24hrs (refresh at 12hrs)	24 hrs (refresh at 12hrs)
Acetone 80%	1hr	2hrs	2hrs	12hrs (refresh at 6hrs)
Acetone 100%	15mins	1hr	2hrs	3hrs
Acetone 100%	15 mins	1hr	2hrs	3hrs
Acetone 100%	15mins	1hr	2hrs	3hrs
50:50 Acetone : infiltration sol.	2hrs	12hrs	12hrs	24hrs
25:75 Acetone : Infiltration sol.		12hrs	12hrs	24hrs
100% Infiltration solution +vacuum	2hrs include opacifying agent	12hrs include opacifying agent	24hrs (refresh at 12 hrs) include opacifying agent at sol. refresh	48hrs (refresh at 24hrs) include opacifying agent at sol. refresh
Embed	24hrs	24hrs	48hrs	48hrs

144
145   Table 1. Showing optimised timings for sample dehydration and embedding for a range of sample sizes

Minimisation of shine-through artefact with an opacifying agent

In MF-HREM, the focal plane of the microscope is the block surface, however when excitatory light is incident on the block surface some light penetrates the block and excites fluorophores deeper in the sample. Emission from these fluorophores beneath the surface is captured as out of focus light and blurs the image particularly in the axial plane. This is the same process which causes blurring for any optical imaging of thick samples, the difference for HREM (and any other serial sectioning block facing technique) being that this light comes only from below the focal plane rather than above and below (see Figure 3A). This leads to a characteristic comet-tail like artefact in the axial imaging plane as seen in Figure 3B. To reduce excitation of fluorophore beneath the block surface, we investigated the addition of an opacifying agent (Orasol Black) to the embedding resin to minimise light transmission through the block.

Orasol Black 45X (Stort Chemicals Ltd, Bishops Stortford, UK) is a carbon-based product used as a dye in printing industries. It was found to be soluble in all resins and organic solvents tested and did not affect the expected staining pattern for any tested stains. The powder was mixed with the resin at the last stage of resin infiltration, prior to positioning and setting the sample within the final block. Once in the block, the dye decreases shine-through by absorbing both incident, excitation light and emitted fluorescence beneath the block's surface.

The transmission spectrum of a relatively low concentration of Orasol Black (see Methods) is shown in Figure 3C. It has a broad absorption in the 450nm to 650nm range, with a steep increase in transmission in the near infrared range (>700nm). We investigated the decrease in shine-through with increasing Orasol Black concentration at a wavelength of 705nm and 600nm, using 3D cell cultures as standardised samples (Figure3B). Analysis of pixel intensity for ROI's drawn around isolated cells allowed fitting of a single exponential decay model (Eq. 1) to the z distance-intensity plot (Figure 3D). estimation of the fit parameters – decay constant (τ), initial intensity (I_0) and the calculation of the half-value layer $T_{1/2} = -\log(2)/\tau$, could then be calculated as well as goodness-of-fit.

$$I = I_0 e^{\tau z} \qquad\qquad\qquad \text{(Eq. 1)}$$

With increasing concentration of Orasol Black, the comet tail artefact appeared reduced and can be quantified by the decrease in both τ and $T_{1/2}$ (see Figure 3E). The initial intensity I_0 also shows a sharp decrease at 8mg/ml, and this can be seen qualitatively in the images as a decrease in the signal and a reduced signal to noise ratio.

The highest Orasol Black concentration (32 mg/ml) provided the greatest decrease in shine-through, but as previously discussed this affected resin polymerisation, causing the resin to set quickly, in some cases, prior to the addition of the secondary catalyst. A balance between minimising shine-through, having good signal to noise and optimum resin setting must therefore be found.

As expected from the transmission spectrum, shine-through was lower for HCS Cell Mask (Em 600 nm) than for HCS Nuclear Mask (Em 705 nm), for the same concentration of Orasol Black (Figure 3F).
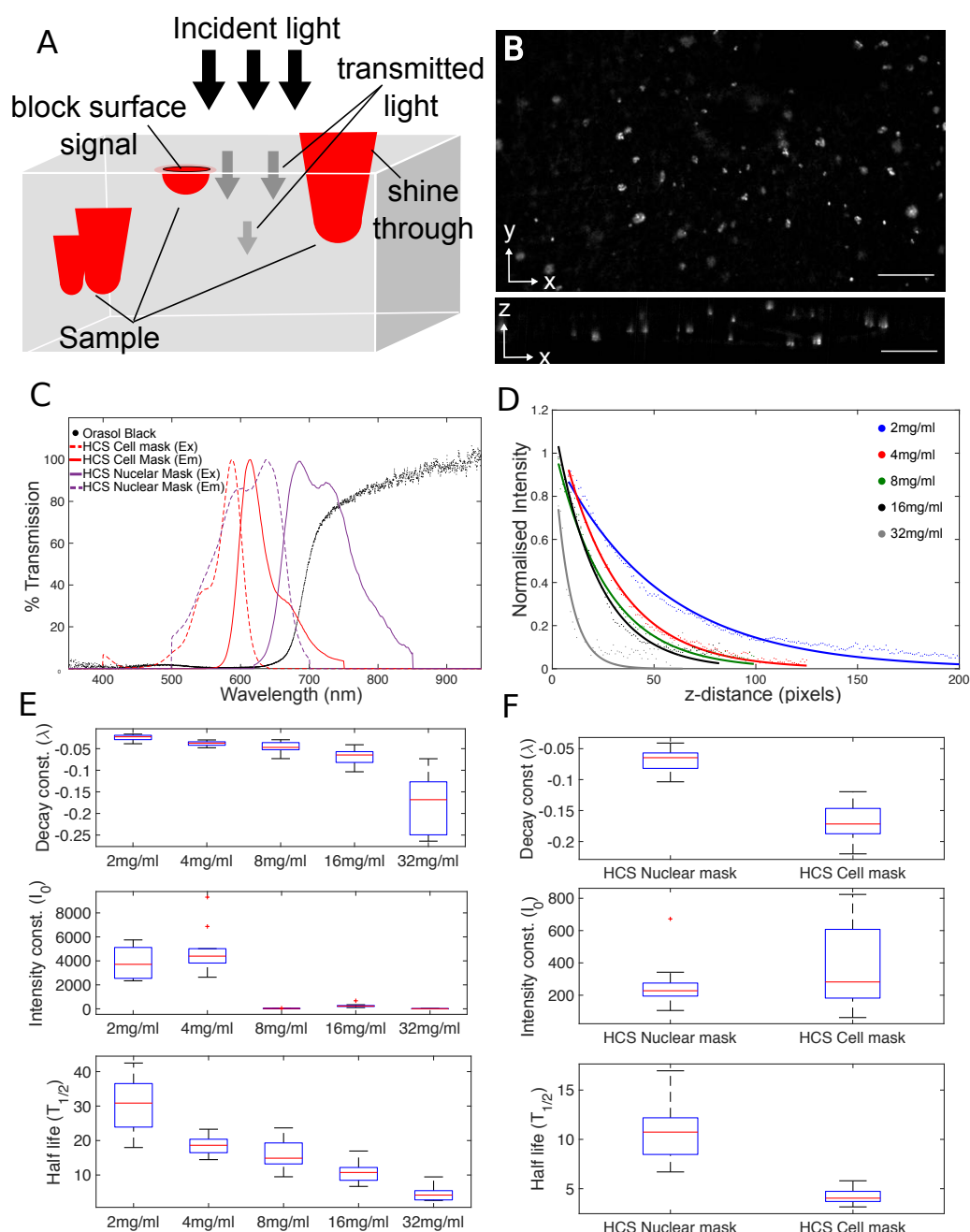
Figure 3. Characterisation of Orasol black as an opacifying agent to reduce shine-through. A) Diagram demonstrating the origin of shine through. B) Showing a representative image of cells in an in vitro 3D culture stained with HCS Nuclear Mask with 16mg/ml of Orasol Black. The comet tail artefact can be seen in the xz plane image, (scale bar is 100 μm). C) Graph showing the measured transmission spectrum of Orasol Black, as well as two tested commercial stains HCS Nuclear Mask and HCS Cell Mask (spectrum from manufacturer). It can be seen that Orasol Black has low transmission in the 400-625 nm range which rises steeply in the 625-700 nm range. The HCS Cell mask spectrum falls almost entirely within the low transmission band of Orasol Black whereas the emission of HCS Nuclear mask falls in the section of steep increase in transmission. D) Showing a single exponential fit to the mean intensity profiles for 10 xz plane ROIs taken of single cells in 3D in vitro cell culture stained with HCS Nuclear Mask of increasing Orasol Black concentration (2,4,8,16,32 mg/ml) R2 values (0.976,0.994,0.989,0.982,0.803) respectively. E) Values of, exponential decay constant (, initial intensity (I0), and half-value layer (T1/2, in microns) are shown for each of the concentrations and show the expected increase in decay constant and half-value layer with increasing Orasol Black concentration. There is also a large decrease in intensity at 8 mg/ml and higher Orasol Black concentrations. F) Shows the same fitting parameters in a comparison between HCS Cell Mask stained sample and HCS Nuclear mask stained sample at 16 mg/ml Orasol Black. As expected from the transmission spectrum the decay constant and half-value layer are smaller in the HCS Cell Mask case than the HCS Nuclear Mask case.

190

191

Minimisation of shine-through artefact with image deconvolution

192

193 To further eliminate shine-through, and maximise the multiplexing potential in MF-HREM, we

194 investigated post-processing strategies to deconvolve the collected signal.

195   For any image, I(x,y,z), we may write:

197
$$I(x, y, z) = O(x, y, z) * h(x, y, z) + n(x, y, z) \hspace{2cm} (\text{Eq. 2})$$

199   where O(x,y,z) the object, is convolved with a point-spread function (PSF), h(x,y,z), and
200   additive noise, n(x,y,z).
201   If the PSF is known and the noise well-estimated the original image can be calculated. The
202   PSF may be: experimentally measured using sub-resolution fluorescent beads, synthetically
203   generated it from known system parameters or estimated via blind deconvolution methods
204   (33).
205   Deconvolution has traditionally been applied to widefield or confocal microscopy
206   where light contamination comes from both above and below the focal plane. For MF-
207   HREM, only light below the focal plane contaminates the image. Thus, the PSF is highly
208   asymmetric, and not well estimated by blind deconvolution techniques or synthetically
209   generated from widely used models. Whilst experimentally measuring the PSF is an option
210   (15), the process is time-consuming and sometimes impossible, as it must be acquired for all
211   wavelengths and magnifications and depends upon having high signal-to-noise ratio with
212   small point-like sources and high similarity between the PSF measuring sample and the
213   actual sample.
214   This is impracticable for many MF-HREM experiments and hence we have used
215   small structures from within the image stack to parameterise a synthetically generated PSF.
216   As opposed to directly using the extracted PSF from the image we use the small object to
217   parameterise a symmetric synthetic PSF, using either Gaussian or diffraction kernels
218   (dependent on the magnification). Zeroing the lower half of these synthetic PSFs then
219   provided a good PSF estimation for deconvolution with high signal to noise ratio. The
220   approach was successfully applied to a number of image stacks at different magnifications,
221   wavelengths and concentrations of Orasol Black. Figures 4B and 4C show the approach for
222   Gaussian kernel extraction and deconvolution for a small section of brain microvasculature,
223   with a diffraction kernel.

225   **Pre-processing to improve signal to noise**
226   The Richardson-Lucy algorithm used to deconvolve the image stacks requires high signal-to
227   -noise ratio for effective deconvolution. Previous researchers have used pre-processing
228   techniques to remove background and reduce noise prior to deconvolution, and this was
229   found to be an important step to achieve effective deconvolution for MF-HREM images (34).
230   The pre-processing methods chosen were motivated by the importance to have processing
231   that could be efficiently applied to large image stacks (>20GB). Median filtering with (1 pixel
232   neighbourhood) was used to remove salt and pepper noise and background subtraction via
233   a rolling-ball algorithm (35,36) was used to remove background from autofluorescence.
234   In addition to these two steps, spectral unmixing was performed for multiplexed staining,
235   prior to deconvolution.
236   Multiplexing fluorescent stains relies on having distinct spectral excitations and emissions,
237   and appropriate microscope filters to differentiate them. In practice, owing to the broad
238   wavelengths over which most fluorophores are excited and emit and the imperfect nature of
239   bandpass filters, spectral cross-talk will occur. Spectral unmixing may be used to effectively
240   separate the contributions, improving image signal-to-noise ratio. Figure 4A shows the
241   improvement in the signal-to-noise for a mouse brain sample that was dual stained for
242   microvascular (Lectin – DyeLight649) and white matter (CMDiI) (emission at 625 nm).

243 Spectral unmixing and background subtraction were performed using freely available
244 ImageJ plugins (further details in Methods) (36). Quantification of line profile signal
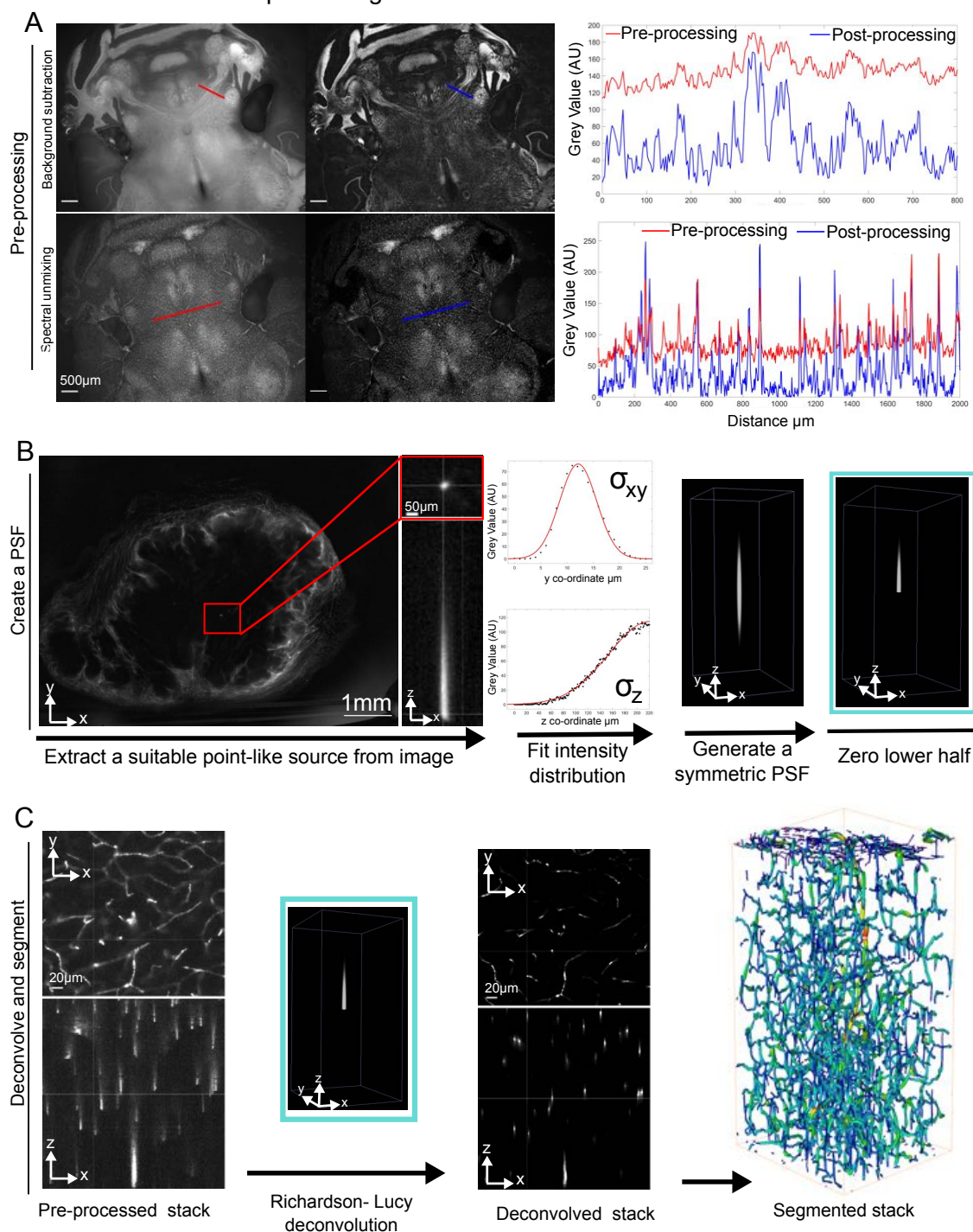245 intensities show the improved signal-to-noise ratio.

Figure 4. The Image processing pipeline. A) Showing the increase in signal-to-noise ratio achieved by pre-processing, using a rolling-ball algortihm to remove autofluorescence (upper row) and spectral unmixing to remove cross talk in multi-fluorescent image stacks (lower row). B) Showing the pipeline for the extraction of a PSF from an image stack of a subcutaneous tumour with microvasculare stained via injection of Lectin-Dyelight649. A suitable point-like source is found in the image stack, this is cropped from the image and a model PSF (in this case 3D gaussian) is fitted to the data. The parameter fits are used in the construction of a synthetic (symmetric) PSF using open source PSF generation with DeconvolutionLab2 (59) and ImageJops (60). This PSF is then half zeroed to create the final PSF. C) The deconvolution of the pre-processed image stack using the PSF. A Richardson-Lucy method with 35 iterations (60) is used to deconvole the stack creating images that can then be segmented and quantified using various methods dependent on the biological context. In this case a MOST tracing algorithm impemented in Vaa3D (40)–(42), (48) is used to segment and skeletonise vascular networks.

246

247 **Compatibility of fluorescent stains with MF-HREM sample preparation**

248 To standardise and increase the speed of testing of fluorescent stains, we used a
249 standardised 3D tissue culture (see Methods for details) to test the compatibility of
250 commercial cell counterstains with the MF-HREM processing steps. Embedding cells in a 3D
251 extra-cellular matrix, and imaging at each stage of dehydration and resin infiltration, allowed
252 straightforward observation of fluorescence quenching or stain-target dissociation in a
253 controllable system. Stains were assessed regularly over a 12-hour period, as it was found
254 that fluorescence quenching often only became apparent after a prolonged period in
255 dehydratant/resin. Table 2 provides a list of tested stains and their compatibility with organic
256 solvents. Counter-stains for cell nucleus, cytoplasm and membrane have been identified.
257 The testing of Neurofilament A antibody shows the importance of correct dehydratant
258 selection, as it can be successfully imaged with an ethanol dehydration but not through
259 acetone dehydration. Also of note is the lipophilic stain CMDiI which is compatible with MF-
260 HREM: this highly useful stain is incompatible with many clearing techniques due to the de-
261 lipidation step (27). Where the standard 3D culture could not easily be used, e.g. for in
262 vivo staining routes or specific antibodies, compatibility was tested on cryosections
263 from stained organs (12).

264

Stain	Fluorescence retain in ethanol	Fluorescece reatained in Acetone	Manufacture/Supplier and catalogue number
Eosin B	Yes	Yes	Sigma 45260
Eosin Y	(Poor solubility)	NT	Sigma 230251
Acridine Orange	Yes	Yes	Sigma A6014
Actin Green™ 488 Ready Probes	No	NT	Thermo Fisher R37110
NucRed™ Live 647 ReadyProbes	No	NT	Thermo Fisher R37106
CellMask™ Orange Plasma membrane Stain	No	NT	Thermo Fisher C10045
HCS CellMask™ Red Stain	Yes	Yes	Thermo Fisher H32712
HCS NuclearMask™ Deep Red Stain	Yes	Yes	Thermo Fisher H10294
DAPI	Yes	No	Sigma Aldrich D9542
Invitrogen™ Lectin GS-II From *Griffonia simplicifolia*, Alexa Fluor™ 647 Conjugate	Yes	Yes	Invitrogen™ L32451
DyLight 649 labeled Lycopersicon Esculentum (Tomato) Lectin (LEL, TL)	Yes	Yes	Vector DL-1178-1
Anti-Neurofilament heavy polypeptide antibody	Yes	No	Abcam ab4680
CellTracker™ CM-DiI Dye	Yes	Yes	Invitrogen C7001
Propidium iodide	yes	NT	Invitrogen P1304MP
SP-DiOC$_{18}$(3) (3,3'-Dioctadecyl-5,5'-Di(4-Sulfophenyl)Oxacarbocyanine, Sodium Salt)	Poor solubility	Poor solubility	Invitrogen D7778
Wheat Germ Agglutinin, Alexa Fluor™ 647 Conjugate	Yes	Yes	Invitrogen W32466
Green fluorescent protein (GFP)	No	No	NA

265
266 Table 2. Detailing trialled stains and their compatibility with ethanol or acetone dehydration

Optimisation of stain penetration into tissue samples

Optical imaging techniques that rely on whole-mount staining (such as MF-HREM), require homogenous and rapid stain penetration, which can be enabled by increasing tissue permeability. We investigated four methods to increase the permeability of tissue samples for use with MF-HREM based on the literature (6,10,37,38): freeze-thaw, proteinase K (P[K]) digestion, iDISCO (which combines several mild detergents (6)) and saponin (N=4). Figure 5 shows the comparison of the four methods and reveals that saponin-treated samples showed significantly greater stain penetration, compared with the control case (p=0.04). The iDISCO method increased stain homogeneity (p=0.055) compared to control kidneys.

Alternative staining routes, in particular i.v. or via transcardiac perfusion, are additional and potentially far faster routes for stain administration in animal models. For vascular staining, use of i.v. injection of fluorescently-conjugated lectins is widely used to stain vasculature throughout the mouse body (8). This technique is transferrable to MF-HREM and in Figure 6, Figure 7 and Figure 8, we show the use of fluorescently conjugated lectin administered via tail vein i.v. in mouse kidney, xenograft tumour and brain respectively. Additionally, using the post-processing tool box we segment and quantify vascular structures in all three cases.
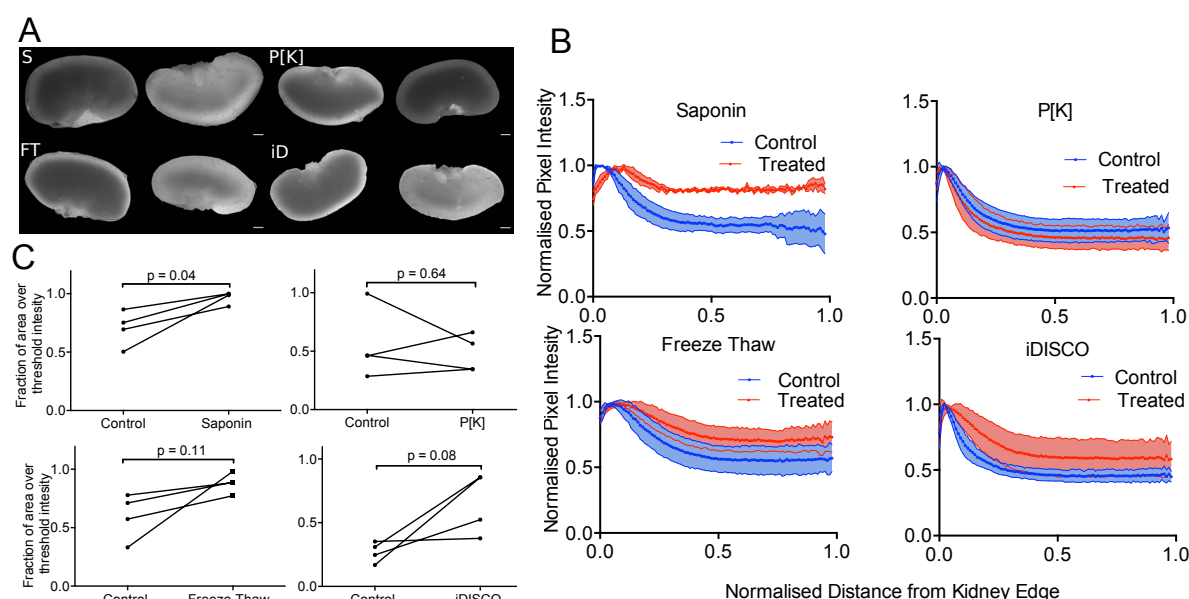

Figure 5. Optimisation of stain penetration in adult mouse kidney samples. Four methods for improving stain penetration are compared: saponin treatment, proteinase [K] digestion, freeze-thaw and iDISCO. For each method, four treated and four control kidneys were investigated, where one kidney from each animal was used as a control for the contralateral kidney. A) shows representative images of the kidneys with the control (contralateral kidney on the left and the treated kidney on the right (scale bar, 1 mm). B) shows the normalised PC-HREM signal intensity profile as a function of radial distance from the kidney centre. C) shows the fractional area of the kidney section image, above a threshold value (the same threshold was used for each treated kidney and matched control). Results of paired t-test analysis demonstrates that saponin treatment significantly increased stain penetration (p<0.05).

Imaging glomeruli in adult mouse kidney with MF-HREM

Having developed the sample processing, image acquisition and post-processing pipeline, we imaged a range of samples to demonstrate the potential utility of MF-HREM and to provide comparison to other 3D optical imaging modalities. The three-dimensional structure of glomeruli, networks of small vessels in the cortex of the kidney, have been shown to be a biomarker of renal and cardiovascular disease (39). Using a lectin-Dyelight649 conjugate (Ex/Em 649/670 nm) to stain glomeruli, we acquired MF-HREM data in wild-type, adult mouse kidneys (Figure 6). After image processing steps described above, glomeruli were

295　segmented using a gradient vector flow segmentation technique implemented in Vaa3D(40–
296　42). This algorithm is a widely used extension to a traditional active contour segmentation
297　technique, where the external energy term in the traditional active contour algorithm is
298　replaced with the gradient vector flow field. After segmentation, the kidney cortex was
299　manually labelled (Figure 6A) and any structures segmented that were not within the cortex
300　were removed. The final step used a connected components analysis and filters any small
301　objects from the data.
302　　　　The MF-HREM analysis revealed a glomeruli distribution that was consistent with
303　their known spatial distribution and with other measures for wild-type (WT) adult mice
304　performed with light sheet or in vivo MRI (39,43) MF-HREM pixel size was 2.17 µm lateral
305　and 2.58 µm axial, enabling identify glomeruli which had a minimum volume of 24×10^5 µm^3.
306

Imaging tumour blood vessels and cell invasion with MF-HREM

308　Tumours have notoriously complex blood vessel networks, and three-dimensional imaging
309　has become a useful method to image their complexity and to study drug delivery (8).
310　Additionally, understanding tumour cell invasion has implication for understanding tumour
311　metastasis and potential treatment targets (44). Figure 7 shows MF-HREM imaging of a
312　subcutaneous xenograft tumour mouse model, initiated from the FaDu human breast cancer
313　cell line. Tumour cells were labelled prior to injection with CM-DiI, a medium-term
314　fluorescent cell-tracking dye that endures for approximately four cell divisions, and is
315　transferred through cell division but not cell-cell contact, (Ex/Em 553/570 nm). Tumour
316　vasculature was stained by i.v. administration of fluorescent Lectin-Dyelight649 (Ex/Em
317　649/670 nm) conjugate. Figure 7A and B show a representative 2D slice with the both stains
318　visible and the 3D reconstruction of the data in both channels.
319　These data reveal the dense, branching vasculature at the periphery of the tumour, and the
320　labelled cells primarily in the tumour centre, which appeared to be non-perfused. The inset
321　to Figure 7A shows yellow arrows marking what seem to be individual or small clusters of
322　cells in a section of tumour where a group of cells is slightly separate from the main tumour
323　bulk.
324　　　　This section of tumour when analysed in 3D with the full MF-HREM pre-processing
325　pipeline (Figure 7C) allows the individual cells to be clearly located (yellow arrows) and their
326　*x,y,z* locations described. Whilst it is unclear whether labelled cells are viable (which would
327　require a different reporter strategy) these results demonstrate the ability of MF-HREM to
328　quantify the 3d location of injected cells in tissue volumes ~1cm^3 several weeks after
329　injection.
330　　　　For the vascular channel, Figure 7D, E and F show the MF-HREM image processing
331　pipeline, with the final vessel segmentation and skeletonisation being carried out using the
332　APP2 algorithm from the Vaa3D neuron tracing plugin (40–42,45). The chaotic nature of the
333　vasculature can be seen from this analysis and such vascular networks can be used in
334　simulations of drug delivery (8) and for understand tumour vessel growth mechanism (46).
335
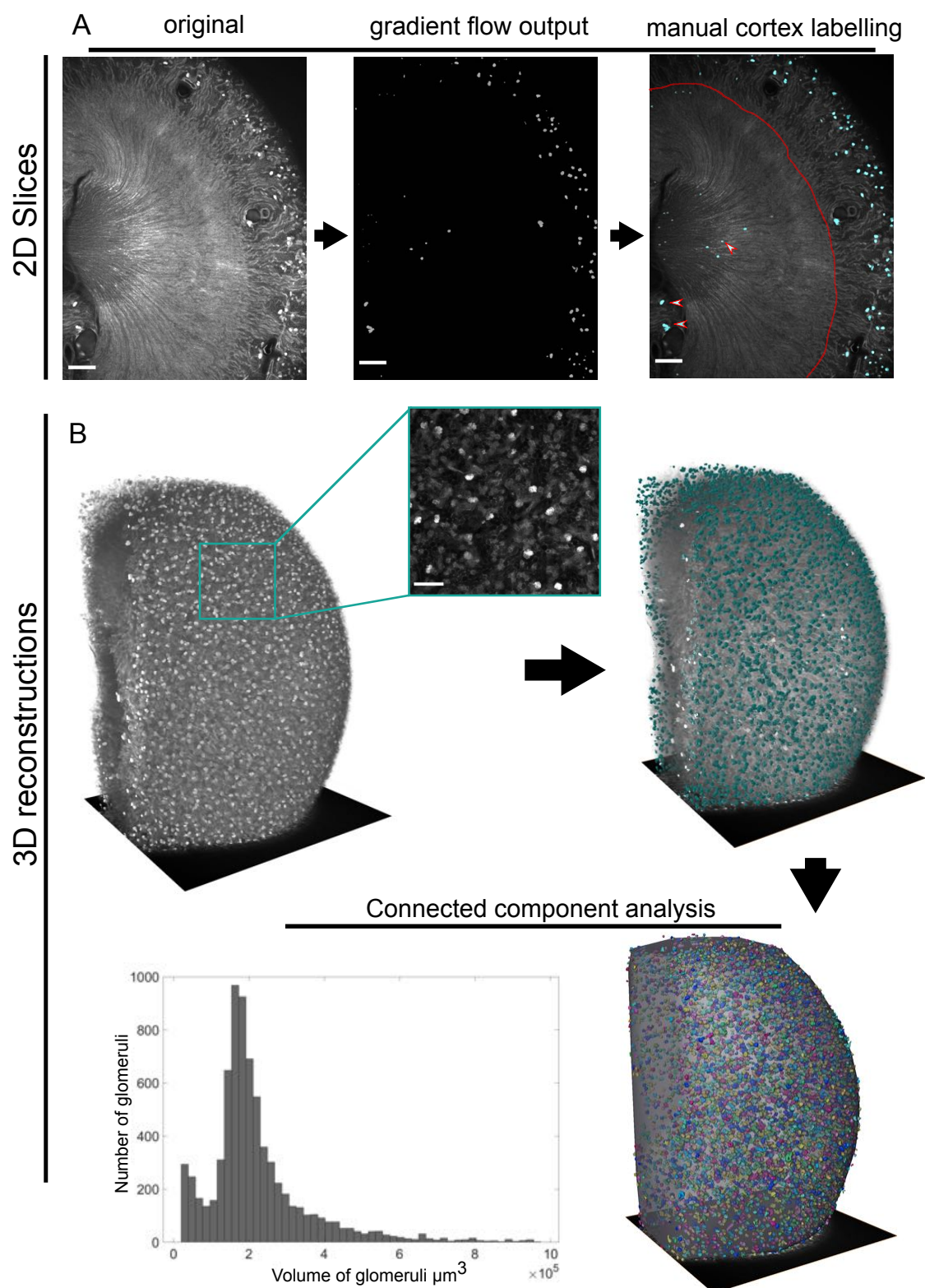
Figure 6. Showing the Lectin-Dyelight649 channel of a multi-stained murine kidney and quantification of glomeruli. A) From left to right 2D slices showing: the original image, the segmentation produced by gradient vector flow algorithm, and finally, the manual correction to remove structures that are segmented (white/red arrows) but fall outside the kidney cortex (red line). Scale bars 500 µm for all 2D slices. B) 3D details of the image processing. The original image stack with inset showing the detail which can be seen on the kidney surface (scale bar 200 µm), then the segmentation via gradient flow algorithm in Vaa3D (40)–(42) and manual exclusion of points not in the cortex. The final step is the outcome of the connected components analysis and hence quantification of glomeruli number, and volume distribution. These data show the expected distribution and size of glomeruli for heathy WT mouse as compared with other techniques(39), (43) .

336
337

Figure 7. Xenograft tumour model analysis. A) Showing a single representative slice with the two stains: CMDiI for injected cell tracking (white), and Lectin-Dyelight 649 c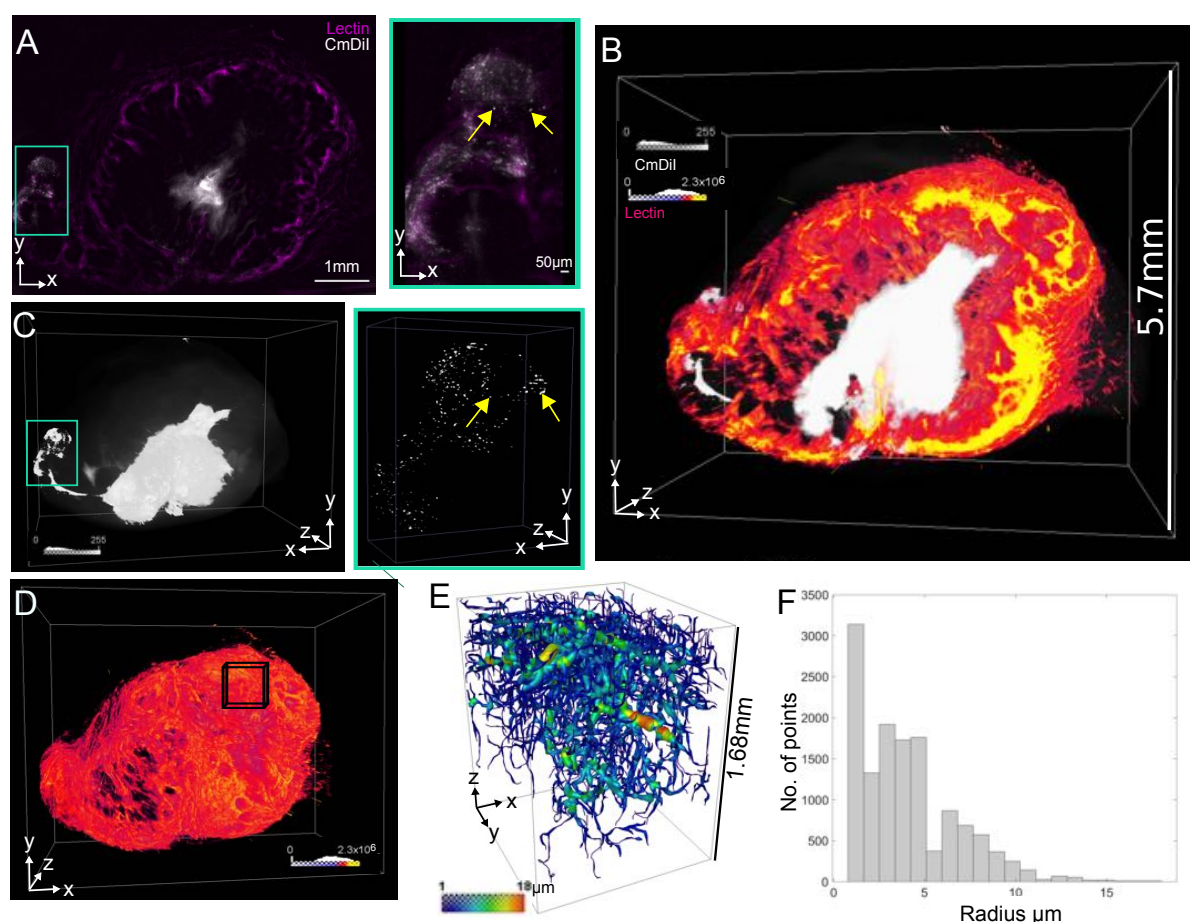onjugate for microvascular staining (magenta). The inset shows a digitally zoomed in portion of the image where small approx. circular structures of cell size are indicated by yellow arrows. B) A 3D rendering of the two channels shows the tumour in its totality with a cut through to show the spatial arrangement of the injected cells within the vascular network. The highly perfused rim can be clearly seen. C) Showing a 3D rendering of the CMDiI channel only and the extent of the cell migration from the initial injecting. The inset shows the same group of cells as in A, deconvolved and rendered in 3D. The yellow arrows indicate the same structures as the 2D case which can more clearly be seen to be single cell or small clusters. The 3D position of these clusters is available from such image data. D) The 3D rendering of the vascular network. E) The extraction and segmentation of a section of the vascular network following the PSF extraction described earlier. In this case the APP2 algorithm from the Vaa3D neuron tracing plugin set was used to segment and skeletonise the deconvolved image stack (40)–(42), (45) . F) Shows the histogram of the vessel radii from E.

338

Imaging brain microvasculature and white matter tracts in a mouse brain with MF-HREM

The three-dimensional spatial distributions of many brain structures including vasculature cells and white matter are of key importance for understanding healthy brain function and changes in these features are used as biomarkers for a large number of neurological pathologies such as Alzheimer's (4,47).

Probing these structures in 3D with MF-HREM can provide insight into many of these conditions and may also provide validation for other clinical imaging tools such as MRI. Figure 8 shows the application of MF-HREM in two instances: where a brain is dual labelled with CMDiI as a white matter-marker and lectin-Dyelight649 as a microvascular stain (figure 8A-E); and where a brain is dual labelled with CMDiI as a white-matter marker and HCS Nuclear Mask as a marker for cell distribution (Ex/Em 638/686) (Figure 8F-8H). Figure 8B shows a high-resolution sub-volume of the vasculature segmented using the MF-HREM processing pipeline and the MOST tracing algorithm implemented in Vaa3D is used. This algorithm is a rayburst sampling algori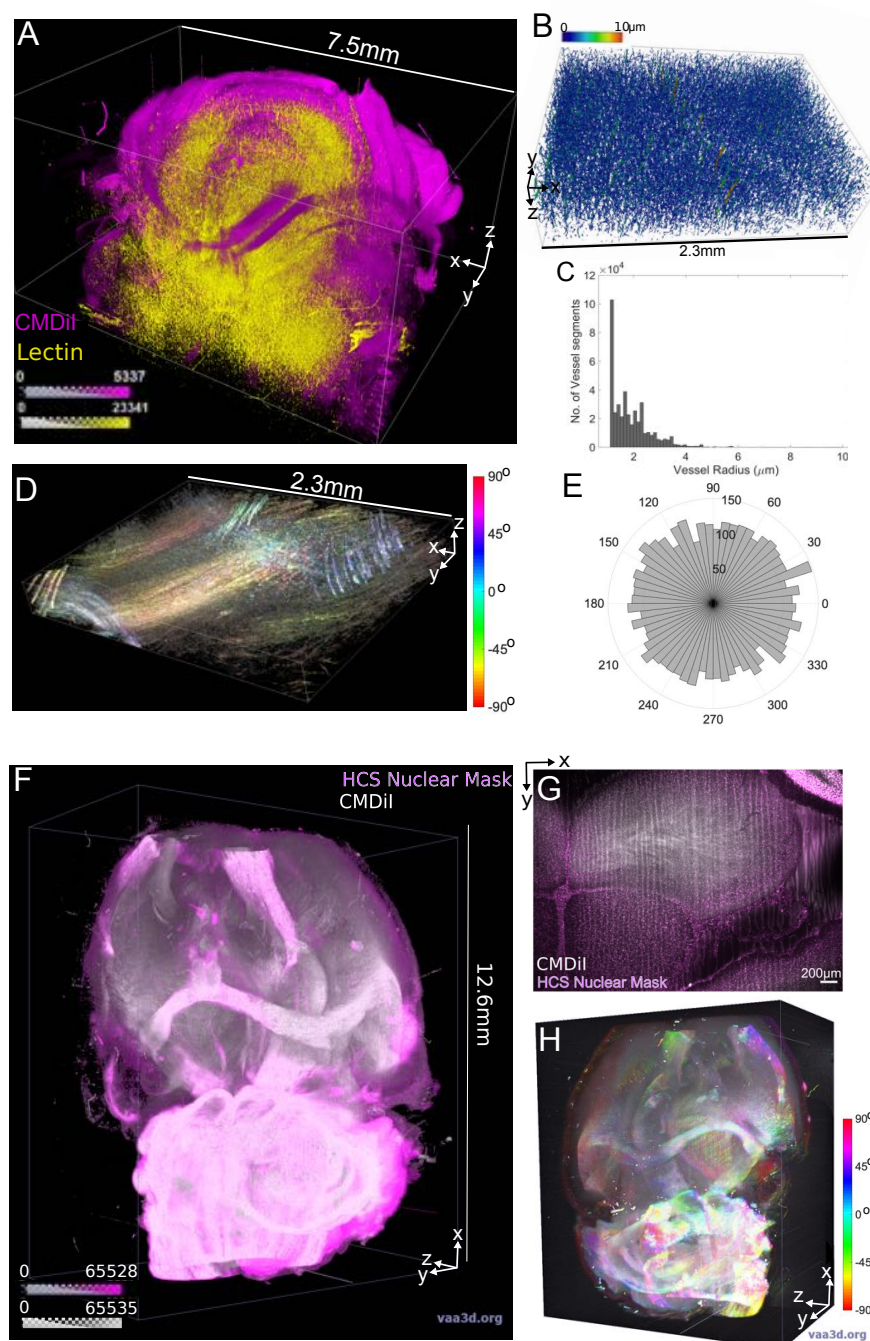thm implemented in a marching fashion (48). The microvasculature can be seen to have a large population of vessels with similar radius (1-4 μm) and a small number of descending vessels with larger radius (~10 μm). This

356   distribution is similar to the mean radius measured in other serial sectioning modalities e.g.
357   MOST (49) and for clearing techniques (50) although no large vessels (>10 µm) are present
358   in MF-HREM data, due to the preferential binding of lectin to microvasculature over larger
359   vessels as noted previously (50).
360   Another important feature of brain microstructure is tissue orientation particularly for
361   white matter which is routinely measured in clinical settings using diffusion weighted MR
362   (DW-MR). This technique measures brain microstructure based on the constrained diffusion
363   of water within the tissue structures. Despite its widespread use for white-matter
364   tractography, the validation of DW-MR is a much discussed issue (51–53). Performing
365   validation requires high-resolution images over large fields of view which must be registered
366   to MR images if quantitative validation is to be performed. Previously CMDiI has been used
367   on individual histological sections of mouse brain to validate tractography from DW-MR
368   (52,54). Whilst this approach is somewhat successful, it is difficult or even impossible to fully
369   align 2D section with the corresponding MR sections. Figure 8D and 8H show white matter
370   orientation. Orientation is calculated from the structure tensor of the image. A Gaussian
371   gradient and 8pxl window size were used in 8D while a 4pxl window size was used in Figure
372   8H to reflect the different pixel sizes of the images. The hue, saturation and brightness
373   denote the orientation, coherence and original image brightness respectively. The colour bar
374   shows the angle represented by the hue. Figure 8E shows a polar histogram of the
375   orientation in Figure 8D where all orientations with a coherence greater than a threshold
376   value of 0.2 are displayed. It can be seen there appears to be an even distribution of local
377   orientations over this sub volume.
378   CMDiI effectively stains white matter tracts due to its lipophilic nature and MF-HREM
379   allows orientation analysis on the entire 3D volume.
380   Such images, particularly the whole brain in Figure 8H, are ideal for validation of MRI
381   tractography data. Tissue clearing techniques are also often unsuitable for this application
382   as lipophilic dyes are often not retained through the de-lipidation stage of clearing protocols
383   (27).
384   In addition to white matter, cell distributions are important markers for development
385   and disease. Figure 8G shows a single slice at a higher magnification from the imaging
386   volume in Figure 8F, cell nuclei can be clearly seen and show Nuclear staining has
387   successfully been retained through processing. Further segmentation requires montaging of
388   higher resolution images.
389
390

Figure 8. MF-HREM of Two brain samples, one stained with CMDiI Ex/Em 553/570nm and Lectin-Dyelight 649 (Ex/Em 649/700) and a second stained with CMDiI and HCS Nuclear Mask (Ex/Em 638/686). A) Showing the volume overlay of both the CMDiI (Magenta) and the Lectin (yellow). Colour bars show pixel intensity. B) Shows a high resolution sub-volume of the vasculature channel successfully segmented and skeletonised using the MF-HREM processing pipeline and the MOST tracing algorithm implemented in Vaa3D. C) Shows the histogram of radii distributions. D) Shows the same sub-volume in the CMDiI-white matter channel, here an orientation analysis has been performed via calculation of the structure tensor of the image using a Gaussian gradient and 8pxl window size. The hue, saturation and brightness denote the orientation, coherence and original image brightness respectively. The colour bar shows the angle represented by the hue. E) Shows a polar histogram of D where all orientations with a coherence greater than a threshold value of 0.2 are displaced. It can be seen there appears to be an even distribution of local orientations over this sub volume. F) Shows a volume overlay of the CMDiI channel (White) and the HCS nuclear mask channel (magenta) for a different brain sample. G) shows a single slice imaged at higher resolution in which nuclei can be clearly seen. H) demonstrates white matter orientation over the whole brain. It was computed as in D but using a smaller window size of 4pxls. The orientation can be seen to clearly follow the expected white-matter tracts.

391

392

Discussion

In this work, we have shown the development of MF-HREM though sample preparation, imaging and image post-processing and quantification. We have demonstrated its applicability in adult mouse organs through a range staining and quantification approaches. Further improvements to MF-HREM are possible in several areas of the imaging pipeline.

398 The resin embedding and staining protocol can be improved by optimisation to a specific
399 biological problem, e.g. a custom mould can be used for staining where the orientation and
400 organ are the same for a large number of samples. Additionally, whilst dehydration and
401 embedding times cannot be easily decreased without compromising the final imaging,
402 automation of the process using an automated histological sample processor could improve
403 consistency and enable faster protocol optimisation for a specific application.
404 Despite the increased stain penetration with saponin treatment, difficulties in segmentation
405 remain primarily due to inhomogeneous staining. Diffusion staining alone will always
406 struggle to achieve homogenous stain penetration in a timely manner but the use of smaller
407 staining molecules such as nanobodies (2) or the use of genetically encoded reporters such
408 as SNAP-CLIP (55), may improve this. Making more use of i.v. staining routes could vastly
409 decrease the time needed for overall sample preparation, however, the large volumes of
410 stain needed for these approaches may be a limiting factor (2).
411 Solving the shine-though artefact is a key challenge for MF-HREM and we have
412 demonstrated two approaches: the inclusion of Orasol Black to physically limit light
413 transmission thorough the sample; and deconvolution using a half zeroed PSF, generated
414 from measurement of the sample stack.
415   Our post-processing method to remove shine-through provides a sample specific
416 PSF, whilst circumventing the problem of poor signal-to-noise that would occur if PSF's were
417 used directly from the image stack. It removes the onerous and impractical requirement to
418 measure the PSF using sub resolution beads for each sample, as wavelength, staining,
419 tissue autofluorescence and many other features are likely to change for each sample.
420 Our method provides a fast and easy to implement alternative that can be effective, as
421 shown in our application to brain and tumour microvasculature.
422 To aid in deconvolution and segmentation, other image-processing approaches such as
423 spectral unmixing (to remove contributions due to spectral overlap in multichannel imaging)
424 and background subtraction via rolling-ball algorithm (to reduce background
425 autofluorescence) were found to improve signal-to-noise ratio, ultimately enabling
426 deconvolution and segmentation. The optimisation of the deconvolution itself is an area that
427 could benefit from further optimisation. In this first instance of MF-HREM use we have used
428 the widely-adopted Richardson-Lucy algorithm with no additional constraints to aid in
429 regularisation, such as a Total-Variation Richardson-Lucy approach, and settled on iteration
430 number via our ability to further segment the data. A fuller investigation into all the
431 parameters and models for deconvolution could further improve and aid in the wider
432 adoption of MF-HREM. In order to make this possible, where specialised post-processing
433 and segmentation algorithms were used, all were from open source software platforms
434 (36,41).
435   Three-dimensional (3D) optical microscopy has been the focus of a substantial body
436 of research, with several new technologies coming to prominence in recent years. This has
437 enabled numerous new biological insights to be made in neuroscience, developmental
438 biology, cancer and immunology (2,6,8,12).
439   Despite the obvious utility of large-volume, high-resolution 3D optical microscopy,
440 there remain many challenges. Clearing protocols can often be complex and lengthy, and
441 the technicality of serial sectioning instruments as well as the long imaging times limit their
442 widespread adoption (3,12). All of these factors cause delays in optimising new protocols,
443 restricts studies to small group sizes and often require specialised imaging facilities. This
444 has created a bottleneck in answering the plethora of potentially important scientific
445 questions which could benefit from 3D imaging.

446   Making large volume high resolution 3D imaging widely available will create faster progress
447   on a range of biological questions and will result in protocols and biological conclusions that
448   are more robust.
449   In this study, we have developed a pipeline for performing MF-HREM, which enables
450   three-dimensional, multiplexed fluorescence imaging of large tissue samples (> 0.5 cm^3), at
451   high resolution. MF-HREM is a block-facing technique, using a commercially available
452   system (Optical HREM, Indigo Scientific, UK), that overcomes shine-through with a
453   combination of a resin opacifying agent (Orasol Black) and image deconvolution. This
454   technique could find wide application through its avoidance of optical sectioning, tissue
455   clearing or the need for a custom built instrument.

Methods

456

Animal models

457

458   All animal studies were licensed under the UK Home Office regulations and the Guidance for
459   the Operation of Animals (Scientific Procedures) Act 1986 (Home Office, London, United
460   Kingdom) and United Kingdom Co-ordinating Committee on Cancer Research Guidelines for
461   the Welfare and Use of Animals in Cancer Research (56)

462

Perfuse fixation

463

464   All animals were euthanized via i.p. injection of 100 mg kg^{-1} sodium pentobarbital
465   (Animalcare, Pentoject) diluted in 0.1 ml phosphate buffered saline (PBS). Once anaesthesia
466   was confirmed, surgical procedures for cardic perfusion were performed for systemic
467   clearance of blood. Heparinized saline (20ml) (0.2 ml, with 1,000 IU ml^{-1}, maintained at
468   37 °C) was administered with a perfusion pump (Watson Marlow, 5058) at a flow rate of
469   3 ml min^{-1} to mimic normal blood flow. After the complete drainage of blood, mice were
470   perfused with 20 ml of 4% paraformaldehyde (PFA, VWR chemicals 4°C). Organs were then
471   removed and fixed for 2-24h in 4% PFA at 4 °C.

472

Murine tumour xenograft model

473

474   Eight- to ten-week-old, female, immune-compromised nu/nu nude mice (background CD1)
475   were used (Charles River Laboratories). Cells from the FaDu human breast cancer cell line
476   (gifted from Dr Craig Murdoch (Sheffield University)) were cultured in complete medium
477   (Dulbecco's minimum essential medium Eagle with L-glutamine (DMEM) (Lonza) + 10% fetal
478   bovine serum (Invitrogen)) in the ratio 1:10 (vol/vol) and incubated at 37 °C and 5% CO_2. To
479   prepare for injection, cells were washed with Dulbecco's phosphate buffered saline and
480   detached with trypsin-EDTA (7–8 min, 37 °C, 5% CO_2) (Sigma). Cells were labelled with
481   CMDiI (Thermofisher UK). Stain was dissolved from stock concentration (1mg/ml in Ethanol)
482   in D-PBS to a working solution of 1 µM. Cells were incubated in the working solution for 5
483   minutes at 37°C, and then for 15 minutes at 4°C. Cells were then washed and re-suspended
484   in PBS for injection. A 100 µl bolus of 1×10^6 cells was injected subcutaneously into the left
485   flank above the hind leg of each mouse (N=5), Non-prestained cells were injected into the
486   right flank. Tumour growth was measured daily with callipers, every day after tumour
487   became palpable, and were grown until total tumour volume was 1500mm^3 or three weeks
488   post-injection has elapsed.

489 For blood vessel staining, 200 µl Lectin (*Tomato*) bound to DyeLyte-649 (Vector UK) (1
490 mg/ml) was administered via tail vein injection and allowed to circulate for 10 minutes before
491 perfusion fixation to allow sufficient binding to the vascular endothelium (8).
492

Stain penetration

494 A variety of mice which had not had procedures that would affect this experiment (e.g. mice
495 with failed subcutaneous tumour induction or those that had been used for MRI sequence
496 tests) were used in order to reduce the number of animals used. All mice were between 10-
497 23 weeks old. They were perfuse fixed as above and both kidneys were removed. Each
498 animal was randomly assigned to one of the four groups (saponin, freeze-thaw, iDISCO and
499 proteinase [K] digestion) and for each animal one kidney was randomly assigned to
500 treatment and the contralateral kidney retained as a matched control. In the saponin,
501 iDISCO and proteinase [K] groups, the control kidney was maintained in PBS and at the
502 same temperature as the treated kidney. For the freeze-thaw group, the control kidney was
503 dehydrated and rehydrated through the same methanol series but with no freeze-thaw
504 cycles applied.
505   Freeze-Thaw: Kidneys were dehydrated through a methanol in dH_2O series: 20%,
506 40%, 60%, 80%, 100% for 1 hr in each (7ml per kidney). Kidneys were freeze-thawed 3
507 times for 20 mins each time at -80 °C. Kidneys were then rehydrated through methanol
508 series 80%,60%,40%,20% ,0% (1 hr each).
509   iDISCO: Kidneys were washed in PTX.2 1hr two times at room temp. Kidneys were
510 incubated overnight at 37°C in a solution containing 1xPBS, 0.2% Triton-X (Sigma UK), 20%
511 DMSO (Sigma UK). Kidneys were then incubated overnight at 37°C in a solution of 1xPBS,
512 0.1% Tween-20 (Sigma UK), 0.1% Triton-X, 0.1% Deoxycholate (Sigma UK), + 0.1% NP40
513 (Sigma UK), 20% DMSO.
514   P[K]: Tris Buffer containing 1.21 g Tris (Sigma UK), 0.147 g $CaCl_2.H_2O$, (Sigma UK),
515 65 ml dH2O, 30 ml glycerol (Sigma UK) was made and 40 µg/mL proteinase [K] (Sigma UK)
516 was added. The sample was incubated at room temp for 10 mins, with constant agitation
517 before being washed on PBS x3 for 10 mins each.
518   Saponin: A solution containing 2 g of gelatin (VWR) in 1 L PBS was made and
519 filtered immediately. After allowing the solution to chill, 5 mL of Triton X-100, 0.1 g of sodium
520 azide (Sigma UK) and 10 mg/ml saponin (Sigma UK) was added to the solution. Kidneys
521 were incubate for (72 hrs) in 3 ml of solution (PBS for control kidneys) at room temp. with
522 constant agitation.
523   After treatment, all kidneys were stained for 94 hrs in HCS Nuclear mask (Thermo
524 Fisher UK) in 40 µl/10ml PBS at room temperature and with constant agitation.
525

Spectroscopy

527 The transmission spectrum of Orasol Black was measured using an HG4000CG-UV-NIR
528 (Ocean Optics) fibre-fed spectrometer. Samples of Technovit 8100 base sol. plus catalyst 1,
529 with a low concentration (0.1 mg/mL) of Orasol Black, were measured in a PMMA semi-
530 micro cuvette over a 4 mm path length, from 350 nm to 95 nm with a QTH10/M (Thorlabs)
531 continuum lamp. The transmission spectrum (Figure 3) has been compensated for the
532 cuvette reflectivity and PMMA absorption.
533

3D standard cell culture samples

Compressed type I collagen hydrogels (RAFT UK) were used as standardized samples for testing stain compatibility with tissue processing and for quantification of shine-through. Samples were prepared in a 24 wellplate using the protocol described by the manufacturer, with the addition of SW1222 colorectal cancer cells at 100,000 cells/mL (57). Samples were fixed with 4% PFA for 20 mins. Post-fixation, cell nuclei were stained with the addition of HCS nuclear mask deep red 2 μL/mL in PBS incubated for 30 mins. Samples were then processed for MF-HREM as described in Table 1.

Resin testing

Multiple candidate resins were tested for setting time, compatibility with opacifying agents final block hardness and quality of cut. Resins used were Technovit 7100 (Heraeus Kulzer, Germany), Technovit 8100 (Heraeus Kulzer, Germany), Spurr resin (Polysciences Inc, USA), LR White (Sigma-Aldrich, USA) and Lowicryl HM20 (Polysciences Inc, USA). Technovit 7100 is a 2-hydroxyethyl methacrylate-based plastic resin, and was prepared using 1 g Technovit 7100 hardener 1 dissolved in 100 mL Technovit 7100 resin. Technovit 7100 hardener 2 was used the catalyze the polymerisation reaction, added in a ratio of 1:15 Hardener 2 to resin.

Technovit 8100 had a similar composition: 0.5 g of Technovit 8100 Hardener 1 dissolved in 100 mL Technovit 8100 resin. The catalyst, Technovit 8100 Hardener 2, was added in a ratio of 1:30 catalyst to resin.

Spurr is an epoxy resin, and was prepared using 4.1 g ERL, 1.43 g diglycidyl ether of polypropylene glycol, 5.9 g nonenylsuccinic anhydride and 0.1 g dimethylaminoethanol accelerator.

LR White is an acrylic resin and was prepared using 2 g benzoyl peroxide accelerator per 100 mL resin.

Lowicryl HM20, a methacrylate resin, was prepared with 0.6% (w/w) benzoyl peroxide accelerator.

Hardness testing was conducted on blocks after they had set using either a Shore durometer D or Shore durometer A. Cut quality was assessed by imaging a block with a mouse kidney embedded using Optical HREM (Indigo Scientific, UK) and counting the number of slices which had areas of flaky resin or voids.

Image post-processing and analysis

Image analysis was carried out using a combination of ImageJ (Fiji distribution)(36), Vaa3D (40–42), Python and Amira.

Shine-through analysis

Shine through analysis was performed in Fiji and Matlab as follows:

Gel image stacks were down-sampled in xy to create isotropic voxels, background subtraction using rolling-ball algorithm with 50 pxl radius, and sliding parabola was used to remove autofluorescent background. Image stacks were resliced into xz stacks. Single isolated cells were manually found in the stack and an ROI was drawn to fully enclose all pixels with intensity above the background. The intensity profile of the ROI was calculated by averaging the intensity over the ROI columns (z-direction). This average signal was truncated at the maximum intensity and fit to a single exponential model in Matlab using a

580   non-linear least squares approach, with start values of 0.5 for $I_0\ and\ \tau$ and limits of ± ∞ (other
581   start values were checked and no difference to final fit parameters was found).
582
583   **Post processing of image stacks:**
584   Spectral unmixing was performed via the Fiji plugin as per the documentation (58).
585   Background subtraction was performed using a rolling-ball algorithm with sliding parabola
586   using a window size dependent on the smallest features of interest in the image stack.
587   Median filtering was performed using the 3D Median filter plugin in Fiji with 1 pxl window size
588   (36).
589   Fitting of a manually extracted PSF to the model was performed in Matlab using the
590   fitting tool box for the case of Gaussian fits. For diffraction kernel PSFs (higher magnification
591   images) FWHM (x,y,z) were measured in the extracted PSFs. To provide a measure of the
592   lateral spread of the PSF the area of the diffraction pattern in the xy plane t two z slices were
593   divided by one another. The first z slice was at the FWHM (z), the second slice was the z
594   slice just before the abrupt change to zero, (i,e. the comet end of the comet-tail artefact).
595   This is the ratio top/bottom used in DeconvolutionLab (59) to parameterise a variety of their
596   synthetic PSFs).
597   The diffraction limited PSF was then generated using ImageJ ops (60) from
598   microscope and sample parameters: sample refractive index RI$_{sample}$ = 1.5 for the sample
599   (refractive index of Technovit 8100), RI$_{immersion}$ = 1.0, NA of 0.25, offset 0 μm working
600   distance 150 μm (default), xy spacing- dependent on sample pixel size, z spacing -
601   dependent on cut thickness, wavelength – sample dependent. This PSF was measured as
602   above and small (50 nm) manual variation in wavelength was used to iteratively optimise the
603   PSF to match the sample.
604   Once a PSF was synthetically generated at the same size as the image stack to be
605   deconvolved the PSF was zeroed in the lower half and background subtracted (pixel
606   intensities less than 0.001 in 32 bit images were zeroed). This PSF was then used in the RL
607   deconvolution algorithm of ImageJ ops using a border size of ¼ the image size in each
608   dimension respectively. Iteration number was tested for each sample and 20 iterations for
609   high magnification to produce adequate deconvolution without noise enhancement. For
610   lower magnification samples 35 iterations was necessary to produce adequate
611   deconvolution and prevent noise enhancement.
612
613   **Kidney Glomeruli segmentation:**
614   Vessel tracing was performed in Vaa3D Gradient Vector Flow algorithm (40–42), with
615   diffusion iteration of 5. Connected component analysis was performed in Amira with a
616   threshold minimum size of 10000 μm^3 based on literature estimates for glomeruli (43). No
617   deconvolution was necessary owing to the size of the structures being imaged, by
618   comparison to the pixel size.
619
620   **Tumour vasculature segmentation:**
621   Tumour images used Gaussian PSF's for deconvolution with parameters of $\sigma_x = \ \sigma_y =$
622    $4\ and\ \sigma_z = 80$ for the Lectin-Dyelight649 channel and $\sigma_x = \ \sigma_y = 4\ and\ \sigma_z = 40$ for the CMDiI
623   channel. Both used 35 iterations of the Richardson-Lucy deconvolution.
624   For tumour vasculature following deconvolution, vascular segmentation was
625   performed using the APP2 algorithm of Vaa3D described previously (40–42,45). Parameter
626   values were Threshold =1(auto thresholding), CNN=3, GSBT was used and other
627   parameters were used at their default values.

Brain Structures:

Brain microvasculature was deconvolved using a diffraction kernel with parameters specified above including xy pixel size of 570 μm and z pixel size of 1720 μm and wavelength of 700 nm. Segmentation was in Vaa3D via the MOST tracing algorithm ,(40–42,48) using a threshold determined by Otsu threshold of 20, seed size 6 and slip size 20. White matter orientation analysis was performed using the OrientationJ plugin of Fiji with a Gaussian gradient and kernel sizes of 8 or 4 for Figures 8D and 8E respectively. HSB images were created with orientation, coherence and original image brightness as the three channels respectively.

HREM imaging

All MF-HREM imaging is carried out using the Optical-HREM instrument (Indigo Scientific, UK). Samples are mounted into the instrument and initially the block are sectioning without imaging to ensure a block surface exactly perpendicular to the optical axis. Once a flat surface is achieved, the desired slice thickness, x,y resolution, focus, total imaging depth, and exposure and gain for each wavelength are set. An air blower and vacuum are positioned to remove serial slices as they are sectioned. Imaging then proceeds in a fully automated manner until the total imaging depth has been achieved.

Acknowledgements

Competing Interests

The authors have no competing interests to declare

References

1.   Hildebrand DGC, Cicconet M, Torres RM, Choi W, Quan TM, Moon J, et al. Whole-brain serial-section electron microscopy in larval zebrafish. Nature. Nature Publishing Group; 2017;545(7654):345.

2.   Cai R, Pan C, Ghasemigharagoz A, Todorov MI, Förstera B, Zhao S, et al. Panoptic imaging of transparent mice reveals whole-body neuronal projections and skull–meninges connections. Nat Neurosci. 2019;22(2):317–27.

3.   Abdeladim L, Matho KS, Clavreul S, Mahou P, Sintes J-M, Solinas, Xavier Arganda-Carreras I, et al. Multicolor multiscale brain imaging with chromatic multiphoton serial microscopy. Nat Commun. Springer US; 2019;in press.

4.   Liebmann T, Renier N, Bettayeb K, Greengard P, Tessier-Lavigne M, Flajolet M. Three-dimensional study of Alzheimer's disease hallmarks using the iDISCO clearing method. Cell Rep. Elsevier; 2016;16(4):1138–52.

5.   Stack EC, Wang C, Roman KA, Hoyt CC. Multiplexed immunohistochemistry, imaging, and quantitation: a review, with an assessment of Tyramide signal amplification, multispectral imaging and multiplex analysis. Methods. Elsevier; 2014;70(1):46–58.

6.   Renier N, Wu Z, Simon DJ, Yang J, Ariel P, Tessier-Lavigne M. iDISCO: a simple, rapid method to immunolabel large tissue samples for volume imaging. Cell. United States; 2014 Nov;159(4):896–910.

7.   Voigt FF, Kirschenbaum D, Platonova E, Pagès S, Campbell RAA, Kastli R, et al. The

674   mesoSPIM initiative: open-source light-sheet microscopes for imaging cleared tissue.
675   Nat Methods. 2019;

676 8.   d'Esposito A, Sweeney PW, Ali M, Saleh M, Ramasawmy R, Roberts TA, et al.
677   Computational fluid dynamics with imaging of cleared tissue and of in vivo perfusion
678   predicts drug uptake and treatment responses in tumours. Nat Biomed Eng.
679   2018;2(10):773–87.

680 9.   d'Esposito A, Nikitichev D, Desjardins A, Walker-Samuel S, Lythgoe MF.
681   Quantification of light attenuation in optically cleared mouse brains. J Biomed Opt.
682   United States; 2015 Aug;20(8):80503.

683 10.   Gleave JA, Lerch JP, Henkelman RM, Nieman BJ. A Method for 3D Immunostaining
684   and Optical Imaging of the Mouse Brain Demonstrated in Neural Progenitor Cells.
685   PLoS One. Public Library of Science; 2013 Aug 6;8(8):e72039.

686 11.   Roberts TA, Hyare H, Agliardi G, Hipwell B, d'Esposito A, Ianus A, et al.
687   Quantitation of brain tumour microstructure response to Temozolomide therapy using
688   non-invasive VERDICT MRI. bioRxiv. 2017 Jan 1;

689 12.   Vigouroux RJ, Belle M, Chédotal A. Neuroscience in the third dimension: Shedding
690   new light on the brain with tissue clearing. Mol Brain. Molecular Brain; 2017;10(1):1–
691   10.

692 13.   Zheng T, Feng Z, Wang X, Jiang T, Jin R, Zhao P, et al. Review of micro-optical
693   sectioning tomography (MOST): technology and applications for whole-brain optical
694   imaging. Biomed Opt Express. Optical Society of America; 2019;10(8):4075–96.

695 14.   Amato SP, Pan F, Schwartz J, Ragan TM. Whole Brain Imaging with Serial Two-
696   Photon Tomography. Front Neuroanat. 2016;10(March):1–11.

697 15.   Krishnamurthi G, Wang CY, Steyer G, Wilson DL. Removal of subsurface
698   fluorescence in cryo-imaging using deconvolution. Opt Express. Optical Society of
699   America; 2010 Oct 7;18(21):22324–38.

700 16.   Seiriki K, Kasai A, Nakazawa T, Niu M, Naka Y, Tanuma M, et al. Whole-brain block-
701   face serial microscopy tomography at subcellular resolution using FAST. Nat Protoc.
702   Springer US; 2019;14(5):1509–29.

703 17.   Gong H, Xu D, Yuan J, Li X, Guo C, Peng J, et al. High-throughput dual-colour
704   precision imaging for brain-wide connectome with cytoarchitectonic landmarks at the
705   cellular level. Nat Commun. Nature Publishing Group; 2016;7:1–12.

706 18.   Anderson RH, Brown NA, Mohun TJ. Insights regarding the normal and abnormal
707   formation of the atrial and ventricular septal structures. Clin Anat. United States; 2016
708   Apr;29(3):290–304.

709 19.   Captur G, Wilson R, Bennett MF, Luxan G, Nasis A, de la Pompa JL, et al.
710   Morphogenesis of myocardial trabeculae in the mouse embryo. J Anat. England; 2016
711   Aug;229(2):314–25.

712 20.   Mohun TJ, Weninger WJ. Embedding embryos for high-resolution episcopic
713   microscopy (HREM). Cold Spring Harb Protoc. 2012;7(6):678–80.

714 21.   Weninger WJ, Geyer SH, Mohun TJ, Rasskin-Gutman D, Matsui T, Ribeiro I, et al.
715   High-resolution episcopic microscopy: a rapid technique for high detailed 3D analysis
716   of gene activity in the context of tissue architecture and morphology. Anat Embryol
717   (Berl). Germany; 2006 Jun;211(3):213–21.

718 22.   Geyer SH, Nöhammer MM, Tinhofer IE, Weninger WJ. The dermal arteries of the
719   human thumb pad. J Anat. 2013;223(6):603–9.

720 23.   Matsui H, Ho SY, Mohun TJ, Gardiner HM. Postmortem high-resolution episcopic
721   microscopy (HREM) of small human fetal hearts. Ultrasound in obstetrics &
722   gynecology : the official journal of the International Society of Ultrasound in Obstetrics

723   and Gynecology. England; 2015. p. 492–3.

724   24.   Rosenthal J, Mangal V, Walker D, Bennett M, Mohun TJ, Lo CW. Rapid high
725   resolution three dimensional reconstruction of embryos with episcopic fluorescence
726   image capture. Birth Defects Res Part C Embryo Today Rev. Wiley Online Library;
727   2004;72(3):213–23.

728   25.   Weninger WJ, Mohun TJ. Three-dimensional analysis of molecular signals with
729   episcopic imaging techniques. Methods Mol Biol. United States; 2007;411:35–46.

730   26.   Tainaka K, Murakami TC, Susaki EA, Shimizu C, Saito R, Takahashi K, et al.
731   Chemical landscape for tissue clearing based on hydrophilic reagents. Cell Rep.
732   Elsevier; 2018;24(8):2196–210.

733   27.   Kim JH, Jang MJ, Choi J, Lee E, Song K--D, Cho J, et al. Optimizing tissue-clearing
734   conditions based on analysis of the critical factors affecting tissue-clearing
735   procedures. Sci Rep. Nature Publishing Group; 2018;8(1):1–11.

736   28.   Chee Tak Yeung E. Plant Microtechniques and Protocols.

737   29.   Marion J, Le Bars R, Satiat-Jeunemaitre B, Boulogne C. Optimizing CLEM protocols
738   for plants cells: GMA embedding and cryosections as alternatives for preservation of
739   GFP fluorescence in Arabidopsis roots. J Struct Biol. The Author(s); 2017;198(3):196–
740   202.

741   30.   Yang Z, Hu B, Zhang Y, Luo Q, Gong H. Development of a Plastic Embedding
742   Method for Large-Volume and Fluorescent-Protein-Expressing Tissues. PLoS One.
743   2013;8(4):4–8.

744   31.   Quester R, Knifka J, Schröder R. Optimization of glycol methacrylate embedding of
745   large specimens in neurological research. Study of rat skull-brain specimens after
746   implantation of polyester meshes. J Neurosci Methods. 2002;113(1):15–26.

747   32.   Gang Y, Liu X, Wang X, Zhang Q, Zhou H, Chen R, et al. Plastic embedding
748   immunolabeled large-volume samples for three-dimensional high-resolution imaging.
749   Biomed Opt Express. Optical Society of America; 2017;8(8):3583–96.

750   33.   Wallace W, Schaefer LH, Swedlow JR. A workingperson's guide to deconvolution in
751   light microscopy. Biotechniques. Future Science; 2001;31(5):1076–97.

752   34.   de Monvel JB, Scarfone E, Le Calvez S, Ulfendahl M. Image-adaptive deconvolution
753   for three-dimensional deep biological imaging. Biophys J. United States; 2003
754   Dec;85(6):3991–4001.

755   35.   Sternberg SR. Biomedical image processing. Computer (Long Beach Calif). IEEE;
756   1983;(1):22–34.

757   36.   Schindelin J, Arganda-Carreras I, Frise E, Kaynig V, Longair M, Pietzsch T, et al. Fiji:
758   an open-source platform for biological-image analysis. Nat Methods. United States;
759   2012 Jun;9(7):676–82.

760   37.   Jafree DJ, Moulding D, Kolatsi-Joannou M, Tejedor NP, Price KL, Milmoe NJ, et al.
761   Spatiotemporal dynamics and heterogeneity of renal lymphatics in mammalian
762   development and cystic kidney disease. Elife. eLife Sciences Publications Limited;
763   2019;8:e48183.

764   38.   Li W, Germain RN, Gerner MY. Multiplex, quantitative cellular analysis in large tissue
765   volumes with clearing-enhanced 3D microscopy (Ce3D). Proc Natl Acad Sci. National
766   Academy of Sciences; 2017;114(35):E7321--E7330.

767   39.   Baldelomar EJ, Charlton JR, Beeman SC, Hann BD, Cullen-McEwen L, Pearl VM, et
768   al. Phenotyping by magnetic resonance imaging nondestructively measures
769   glomerular number and volume distribution in mice with and without nephron
770   reduction. Kidney Int. United States; 2016 Feb;89(2):498–505.

771   40.   Peng H, Bria A, Zhou Z, Iannello G, Long F. Extensible visualization and analysis for

772   multidimensional images using Vaa3D. Nat Protoc. England; 2014 Jan;9(1):193–208.

773   41.   Peng H, Ruan Z, Long F, Simpson JH, Myers EW. V3D enables real-time 3D
774   visualization and quantitative analysis of large-scale biological image data sets. Nat
775   Biotechnol. Nature Publishing Group; 2010;28(4):348.

776   42.   Peng H, Tang J, Xiao H, Bria A, Zhou J, Butler V, et al. Virtual finger boosts three-
777   dimensional imaging and microsurgery as well as terabyte volume image visualization
778   and analysis. Nat Commun. 2014;5(1):4342.

779   43.   Klingberg A, Hasenberg A, Ludwig-Portugall I, Medyukhina A, Männ L, Brenzel A, et
780   al. Fully Automated Evaluation of Total Glomerular Number and Capillary Tuft Size in
781   Nephritic Kidneys Using Lightsheet Microscopy. J Am Soc Nephrol. American Society
782   of Nephrology; 2017;28(2):452–9.

783   44.   Friedl P, Wolf K. Tumour-cell invasion and migration: diversity and escape
784   mechanisms. Nat Rev Cancer. 2003;3(5):362–74.

785   45.   Xiao H, Peng H. APP2: automatic tracing of 3D neuron morphology based on
786   hierarchical pruning of a gray-weighted image distance-tree. Bioinformatics. England;
787   2013 Jun;29(11):1448–54.

788   46.   Magdeldin T, López-Dávila V, Pape J, Cameron GWW, Emberton M, Loizidou M, et
789   al. Engineering a vascularised 3D in vitro model of cancer progression. Sci Rep.
790   Nature Publishing Group; 2017;7(October 2016):1–9.

791   47.   Bennett RE, Robbins AB, Hu M, Cao X, Betensky RA, Clark T, et al. Tau induces
792   blood vessel abnormalities and angiogenesis-related gene expression in P301L
793   transgenic mice and human Alzheimer{\textquoteright}s disease. Proc Natl Acad Sci.
794   National Academy of Sciences; 2018;115(6):E1289--E1298.

795   48.   Ming X, Li A, Wu J, Yan C, Ding W, Gong H, et al. Rapid reconstruction of 3D
796   neuronal morphology from light microscopy images with augmented rayburst
797   sampling. PLoS One. Public Library of Science; 2013 Dec 31;8(12):e84557–e84557.

798   49.   Zhang X, Yin X, Zhang J, Li A, Gong H, Luo Q, et al. High-resolution mapping of brain
799   vasculature and its impairment in the hippocampus of Alzheimer's disease mice. Natl
800   Sci Rev. 2019;6(6):1223–38.

801   50.   Todorov MI, Paetzold JC, Schoppe O, Tetteh G, Efremov V, Völgyi K, et al.
802   Automated analysis of whole brain vasculature using machine learning. bioRxiv. Cold
803   Spring Harbor Laboratory; 2019;613257.

804   51.   Jelescu IO, Budde MD. Design and Validation of Diffusion MRI Models of White
805   Matter. Front Phys. 2017;5(November).

806   52.   Budde MD, Frank JA. Examining brain microstructure using structure tensor analysis
807   of histological sections. Neuroimage. 2012;63(1):1–10.

808   53.   Alexander DC. Modelling, Fitting and Sampling in Diffusion MRI BT - Visualization
809   and Processing of Tensor Fields: Advances and Perspectives. In: Laidlaw D, Weickert
810   J, editors. Berlin, Heidelberg: Springer Berlin Heidelberg; 2009. p. 3–20.

811   54.   Grussu F, Schneider T, Yates RL, Zhang H, Wheeler-Kingshott CAMG, DeLuca GC,
812   et al. A framework for optimal whole-sample histological quantification of neurite
813   orientation dispersion in the human spinal cord. J Neurosci Methods. 2016;273:20–
814   32.

815   55.   Kohl J, Ng J, Cachero S, Ciabatti E, Dolan M-J, Sutcliffe B, et al. Ultrafast tissue
816   staining with chemical tags. Proc Natl Acad Sci. National Academy of Sciences;
817   2014;111(36):E3805--E3814.

818   56.   Workman P, Aboagye EO, Balkwill F, Balmain A, Bruder G, Chaplin DJ, et al.
819   Guidelines for the welfare and use of animals in cancer research. Br J Cancer. Nature
820   Publishing Group; 2010;102(11):1555–77.

821   57.   Lonza. RAFT 3D cell culture kit protocol [Internet]. [cited 2020 Mar 7]. Available from:
822   https://bioscience.lonza.com/lonza_bs/CH/en/raft-3d-cell-culture

823   58.   Walter J. Spectral Unmixing Plugin. imageJ; 2006.

824   59.   Sage D, Donati L, Soulez F, Fortun D, Schmit G, Seitz A, et al. DeconvolutionLab2:
825   An open-source software for deconvolution microscopy. Methods. 2017;115:28–41.

826   60.   Rueden, C., Dietz, C., Horn, M., Schindelin, J., Northan, B., Berthold, M. & Eliceiri K
827   (2016). ImageJ Ops. 2016.

828